Bio-Design and Manufacturing (2025) 8:976–993
https://doi.org/10.1631/bdm.2500026

RESEARCH ARTICLE

Bone marrow mesenchymal stem cell-loaded HAMA hydrogel within highly bionic nerve guidance conduits for peripheral nerve regeneration

Chao Li[1,3,4] · Li-Fang Zhu[2] · Ming-Wei Chang[5] · Hao Li[6] · Shiheng Liu[1,3,4] · Baolin Wang[1,3,4]

Received: 21 January 2025 / Accepted: 3 June 2025 / Published online: 14 November 2025

Abstract

Nerve guidance conduits (NGCs) effectively support and guide the regeneration of injured nerves. However, traditional NGCs often lack essential growth factors and fail to create a biomimetic microenvironment conducive to nerve regrowth. This study develops a highly bionic nerve guidance conduit (HB-NGC) using hybrid high-voltage electrotechnologies that integrate electrospinning with electrohydrodynamic (EHD) printing. The outer layer consists of electrospun polycaprolactone fibers loaded with carboxyl-multi-walled carbon nanotubes, while the inner layer is composed of highly aligned polycaprolactone fibers created by EHD printing. The tubular core of the HB-NGC is filled with hyaluronic acid methacryloyl (HAMA) hydrogel encapsulating bone marrow mesenchymal stem cells (BMSCs). This highly biomimetic NGC is conductive, capable of guiding axon growth, and sustainably releases growth factors, effectively mimicking the structure, function, and characteristics of natural peripheral nerves. Its distinctive architectural layers provide an exceptional bionic microenvironment by restoring physical pathways, facilitating electrical signal conduction, and supplying an extracellular matrix (ECM) environment enriched with essential growth factors. Additionally, the HB-NGC's morphology, along with its physicochemical and mechanical properties, effectively bridges the gap between severed nerve ends. In vivo animal studies validate the HB-NGC's effectiveness, highlighting its significant potential to enhance peripheral nerve regeneration.

✉ Ming-Wei Chang
m.chang@ulster.ac.uk

✉ Baolin Wang
baolinwang@hebut.edu.cn

[1] State Key Laboratory of Reliability and Intelligence of Electrical Equipment, Hebei University of Technology, Tianjin 300401, China

[2] College of Tourism and Leisure Management, Fujian Business University, Fuzhou 350012, China

[3] Tianjin Key Laboratory of Bio-electromagnetic and Neural Engineering, Hebei University of Technology, Tianjin 300132, China

[4] Hebei Key Laboratory of Bioelectromagnetics and Neuroengineering, School of Health Sciences and Biomedical Engineering, Hebei University of Technology, Tianjin 300132, China

[5] Nanotechnology and Integrated Bioengineering Centre, University of Ulster, Belfast BT15 1AP, UK

[6] Key Laboratory of Molecular Biophysics of Hebei Province, School of Health Sciences and Biomedical Engineering, Hebei University of Technology, Tianjin 300401, China

Graphical abstract

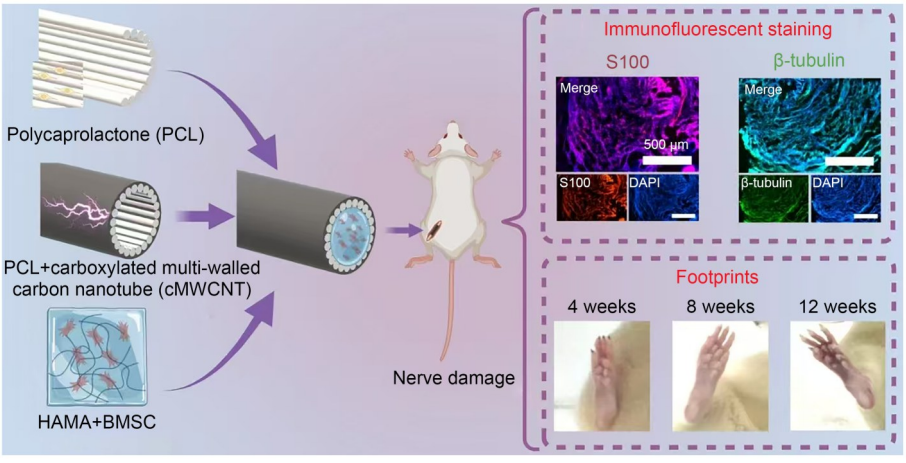

Keywords Bionic · Bone marrow mesenchymal stem cells (BMSCs) · Hyaluronic acid methacryloyl (HAMA) hydrogel · Long distance · Peripheral nerve regeneration

1 Introduction

Peripheral nerve injury (PNI) is a relatively common condition resulting from various causes, such as trauma and surgical procedures [1]. The impact of PNI extends far beyond the immediate effects of the injury, significantly affecting long-term health outcomes, daily functioning, and overall quality of life [2, 3]. Peripheral nerves are essential for transmitting signals between the brain, spinal cord, and the rest of the body; damage to these nerves can lead to a range of clinical symptoms, including sensory disturbances, motor deficits, and autonomic dysfunction [4]. These impairments can cause partial or complete disability, necessitating extensive medical intervention and rehabilitation, while also negatively impacting economic productivity [5]. Although some nerves can regenerate spontaneously, many cases of PNI require complex surgical procedures or innovative regenerative therapies to restore function, which may not always achieve optimal outcomes [6–8].

Nerve guidance conduits (NGCs) have emerged as a promising alternative to autografts for nerve repair. NGCs provide a customized and scalable solution, as they can be manufactured in various sizes and shapes to meet specific clinical needs [9–11]. Unlike autografts, which require complex surgical procedures to harvest a suitable donor nerve, NGCs eliminate the need for a secondary surgical site, thereby reducing surgical complexity, minimizing the risk of complications, and enhancing patient recovery [12, 13]. Currently, the U.S. Food and Drug Administration has approved several neural conduits, primarily composed of collagen (K011168, K012814, K130557, and K163457) and chitosan (K143711 and K180222) [14]. Likewise, China's National Medical Products Administration (NMPA) has authorized multiple neural conduits (20163132399 and 20203130898) [14]. However, the majority of these clinically available options feature a simple hollow tubular structure, which substantially limits their regenerative performance. To address these shortcomings, the development of next-generation NGCs with enhanced structural, biological, and functional properties remains a key research priority. Some NGCs are also engineered with growth factors or extracellular matrix (ECM) components to further enhance their regenerative capabilities [15–17]. Additionally, NGCs have demonstrated effectiveness in situations where autografts may be less viable, such as bridging longer nerve gaps, repairing mixed or motor nerves, or treating patients with limited availability of donor nerves.

Peripheral nerve repair is a complex and dynamic process due to multiple interrelated factors, involving the intricate structure and function of nerves. Unlike other tissues in the body, nerve cells (neurons) have a limited ability to regenerate, and this process is often incomplete, particularly over long distances or in suboptimal environments. Recent research focuses on biomimetic conduits that mimic the natural architecture of nerve bundles, guiding cell migration through highly directional multi-groove and multi-channel systems to create supportive microenvironments and promote a multi-phase healing process [18, 19]. This approach enhances the speed and quality of neural repair by regulating the nerve regeneration process [20–23].

However, nerve regeneration is inherently slow, and NGCs loaded with growth factors face challenges, such as the limitations of using single growth factors, unstable release, rapid inactivation, and potential toxic side effects from

overdosing [24]. Stem cells offer a promising approach for peripheral nerve repair. Studies have shown that stem cells exert their therapeutic effects through two principal pathways. First, they secrete a spectrum of neurotrophic factors (e.g., nerve growth factor and brain-derived neurotrophic factor), which create a pro-regenerative microenvironment, enhancing axonal growth and Schwann cell activation [25]. Second, while stem cells possess the capacity to differentiate into neural lineages (including Schwann-like cells and neurons), this process requires specific induction protocols and occurs with limited efficiency in vivo. Bone marrow-derived mesenchymal stem cells (BMSCs), in particular, demonstrate limited spontaneous differentiation capacity in non-inductive microenvironments, suggesting that their therapeutic benefits are predominantly mediated through paracrine mechanisms [26, 27]. By secreting multiple growth factors in a sustained and regulated manner, BMSCs support stable and effective nerve regeneration [28, 29]. The targeted encapsulation and delivery of stem cells are critical to this approach, ensuring their viability and effective delivery throughout the therapeutic process. Additionally, natural nerves transmit signals and control physiological functions through the conduction of electrical signals, which is essential for restoring nerve function [30–33].

Electrohydrodynamic (EHD) printing technology, which allows precise control of the print trajectory, is widely used to prepare highly aligned NGCs [34]. Carboxylated multiwalled carbon nanotubes (cMWCNTs) exhibit excellent electrical conductivity and are extensively employed in the preparation of conductive devices for implantation [35, 36]. Hydrogels, characterized by their high water content and ECM-like structure [37], are favorable for cell proliferation and growth [38]. Because hyaluronic acid is a primary component of the ECM, hyaluronic acid methacryloyl (HAMA) hydrogels derived from it can reduce immune rejection and are frequently used for cell delivery into the body [39]. Moreover, the ECM-like properties of hydrogels help enhance the paracrine function of stem cells [40, 41]. However, there are limitations in integrating these advantages to develop functional NGCs that create a biomimetic microenvironment and overcome challenges during peripheral nerve repair.

In this study, a highly bionic nerve guidance conduit (HB-NGC) with a distinctive bundle structure is developed using hybrid high-voltage technologies. The outer layer consists of electrospun polycaprolactone (PCL) fibers loaded with cMWCNTs, which make it electrically conductive and capable of restoring neuroelectric signal conduction in damaged nerves [42]. The inner layer is composed of aligned PCL fibers fabricated through EHD printing, providing directional guidance via groove structures for the growth of Schwann cells and mitigating nerve mismatch, closely resembling the natural architecture of peripheral nerve fibers. The tubular core of the HB-NGC is filled with HAMA hydrogel loaded with BMSCs. Previous studies have reported that HAMA hydrogel typically degrades within approximately 30 d in vitro and can sustain therapeutic effects for up to 12 weeks when loaded with stem cells [42]. The schematic of the preparation process for the HB-NGC is shown in Fig. 1. This configuration enables the target release of various nerve regeneration-related growth factors through paracrine signaling, accelerating the nerve repair process and effectively stimulating the function of natural nerves. During the preparation of HB-NGC, several conduits were

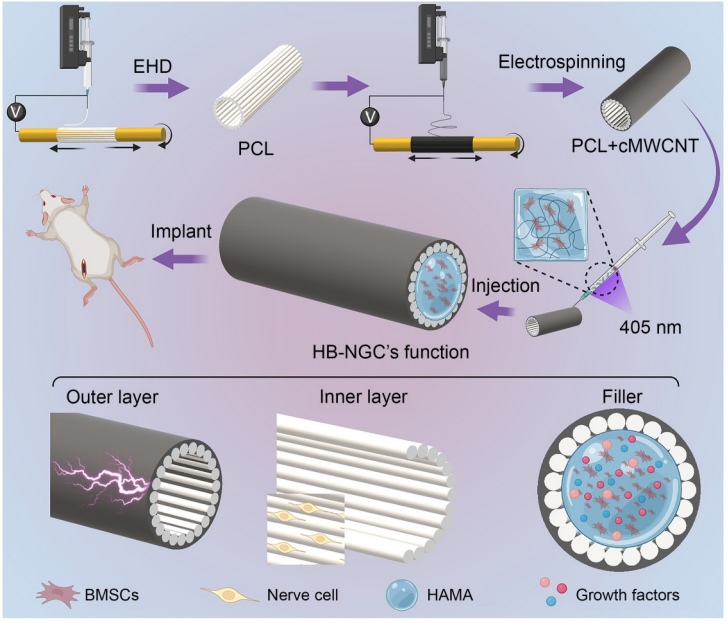

Fig. 1 Schematic representation of the fabrication and functional mechanism of the HB-NGC

prepared for comparison: an unfilled HAMA hydrogel conduit (NGC), a conduit filled only with HAMA hydrogel (NGC+HAMA), and a conduit filled with HAMA hydrogel loaded with BMSCs (NGC+HAMA (BMSCs)). The results demonstrate that the functional HB-NGC facilitates electrical transmission and significantly promotes the regeneration and recovery of the sciatic nerve in rats, highlighting its promising potential for clinical applications.

2 Experimental section

2.1 Materials

PCL (Mw≈80 000; 440744) and glacial acetic acid (GAA, A116172) were purchased from Sigma-Aldrich (St. Louis, MO, USA). cMWCNTs (100232) were sourced from Jiangsu Xianfeng Nano Material Technology Co., Ltd. (China). Dichloromethane (DCM, D824411) was obtained from Macklin Biochemical Co., Ltd. (Shanghai, China). HAMA (EFL-HAMA-400K) and lithium phenyl-2,4,6-trimethylbenzoylphosphinate (LAP, EFL-LAP) were purchased from EFL-Tech (Suzhou) Co., Ltd. (China). All materials were used as received without further purification. Dulbecco's modified Eagle's medium (DMEM) was purchased from CORNING (USA). Heat-inactivated fetal bovine serum (FBS) was obtained from Zhejiang Tianhang Biotechnology Co., Ltd. (China). Additionally, penicillin-streptomycin mixture, L-alanyl-L-glutamine, and sodium pyruvate were purchased from Shanghai Zhongqiao Xinzhou Biotechnology Co., Ltd. (China). Phalloidin was provided by Shanghai Yeasen Biotechnology Co., Ltd. (China), and 4',6-diamidino-2-phenylindole (DAPI) was supplied by Beijing Solarbio Science & Technology Co., Ltd. (China).

2.2 Extraction and culture of BMSCs

BMSCs were isolated using the whole bone marrow extraction method [43]. Four-week-old male Sprague–Dawley (SD) rats were euthanized by cervical dislocation and immersed in 75% ethanol for disinfection twice, for 5 min each time. The rats were then placed on a sterile workbench, and an incision was made in the inguinal region to expose the leg muscles. The legs were detached at the joints, and most of the muscle and fascia were removed using ophthalmic scissors. The remaining tissue was cleaned with sterile gauze and rinsed with phosphate-buffered saline (PBS). Subsequently, the epiphyses were excised to expose the bone marrow cavity. A 1-mL syringe was used to flush the bone marrow cavity with a complete DMEM (1.0 g/L glucose) containing 10% FBS into a culture dish. This flushing process was repeated three times in each direction until the wash solution appeared clear. The collected wash solution was then centrifuged at 1000 r/min for 5 min, and the supernatant was discarded. The cell pellet was resuspended in complete medium and transferred to a cell culture flask, which was then incubated at 37 °C with 5% CO_2. The complete medium comprised 87% DMEM (1.0 g/L glucose), 10% FBS, 1% penicillin-streptomycin solution, 1% L-alanyl-L-glutamine, and 1% sodium pyruvate. For the experiments, cells in the logarithmic growth phase and at passages P2–P6 were used.

2.3 Preparation of BMSCs-loaded HAMA hydrogels

A light-shielded environment was maintained to prepare a 0.25% (2.5 g/L) initiator standard solution. The desired mass of HAMA was then combined with this initiator solution in a sealed, light-shielded container and stirred at room temperature (25 °C) for 1.5 h until complete dissolution was achieved, resulting in a 1% (0.01 g/mL) HAMA solution. The HAMA concentration was determined based on the manufacturer's recommendations and further optimized through preliminary testing to ensure adequate gel formation and functional support in this study. This solution was sterile-filtered using a 0.22-μm filter to ensure sterility. BMSCs were utilized for experiments once they reached 80% confluency. After discarding the culture medium and washing with PBS, the cells were digested with 0.25% trypsin-ethylenediaminetetraacetic acid (EDTA) and then resuspended in the HAMA solution to achieve a final cell density of 1×10^5 cells/mL. The cell-containing precursor solution was transferred to a sterile syringe and exposed to a 405-nm portable curing light (35 mW/cm^2) for 30 s, converting the precursor solution into cell-loaded HAMA hydrogels, which were then ready for subsequent injection and filling of conduits.

2.4 Preparation of electrospinning and EHD printing solutions

A 10% (mass fraction) PCL solution was prepared by dissolving PCL in DCM. To create the outer layer of the nerve conduits, 5% (mass fraction) cMWCNTs, based on the weight of PCL, were incorporated into the PCL solution. This mixture was thoroughly stirred using a magnetic stirrer (VELPARE, Italy) at a constant speed of 300 r/min for 2 h at 25 °C to achieve a uniform solution for electrospinning. Additionally, a 25% (mass fraction) PCL solution was prepared by dissolving a specific mass of PCL in GAA. This solution was uniformly stirred at a constant speed of 600 r/min for 5 h at 25 °C to prepare it for EHD printing. Specifically, the electrical conductivities of the PCL solution and PCL doped with 5% cMWCNTs were measured using a FiveEasy Plus^{TM} (METTLER TOLEDO, USA) benchtop conductivity meter [34].

2.5 Preparation of HB-NGC

The HB-NGC consists of an inner layer made of highly aligned PCL fibers, prepared using EHD printing technology, and an outer layer composed of a PCL film loaded with cMWCNTs, fabricated via electrospinning. The cavities of the HB-NGC were then injected and filled with HAMA hydrogel loaded with BMSCs.

Inner layer: A low-speed rotating drum collector was used to collect the EHD-printed fibers. The drum was positioned on the EHD printing platform, with the collection rod and needle adjusted to a 10-mm distance along the *Z*-axis and aligned at 0 mm along the *X*-axis. The platform was programmed to move repeatedly along the *Y*-axis, covering a range of 10–40 mm at a speed of 50 mm/min, while the drum rotated at 0.5 r/min. The 25% PCL solution was EHD-printed for 40 min to create the highly aligned inner layer. During this process, the flow rate of the PCL solution was maintained at 55 μL/h, and the voltage was set at 1.58 kV.

Outer layer: The drum rotation speed was set to 50 r/min, with the distance between the collector rod and the needle adjusted to 7 cm along the *Z*-axis. Electrospinning of the outer layer was conducted for 20 min. The flow rate during electrospinning was maintained at 1000 μL/h, and the voltage was set to 6.26 kV.

Filler: To prepare an NGC filled internally with HAMA hydrogel, 0.2 mL of HAMA hydrogel was injected into the tubular core of the NGC. Subsequently, 0.2 mL of HAMA hydrogel containing BMSCs was injected into the NGC inner core to create a nerve guidance conduit filled internally with BMSCs-loaded HAMA hydrogel.

2.6 Scanning electron microscopy (SEM) analysis

The morphology of the HB-NGC was examined using a scanning electron microscope (TESCAN GAIA3, Czech Republic). Before scanning, the NGC+HAMA samples were cryofractured in liquid nitrogen and freeze-dried for 48 h using a freeze dryer (DYYB-10, Shanghai Deyang Instrument Co., Ltd., China). Gold sputtering was performed on the samples using ion sputtering equipment (EDT-900, Vision Precision Instruments, China) at a current intensity of 10 mA for 60 s. SEM images were then acquired, and ImageJ software (National Institutes of Health, Bethesda, Maryland, USA) was used to analyze and statistically evaluate the diameters of the aligned inner layer fibers, the electrospun fiber diameters, and the porosity of the HAMA hydrogel.

2.7 Fourier transform infrared spectroscopy (FTIR) analysis

The composition and interactions between components of the HB-NGC were characterized using FTIR (Bruker, Switzerland). Spectra were recorded over a range of 4000 to 400 cm^{-1} with a scan frequency of 16 Hz.

2.8 Water contact angle analysis

The hydrophilicity of the inner, outer, and filler surfaces of the HB-NGC was evaluated using a Drop Shape Analyzer (DSA30, KRUSS, Germany). A 5-μL drop of distilled water was placed on each surface, and the water contact angles were measured using the sessile drop method. Hydrophilicity was statistically analyzed across the samples. Three samples were prepared for each group, and three measurements were taken for each sample.

2.9 Mechanical property analysis

Axial tensile tests were conducted on the highly aligned PCL inner layer and the NGC using a moving clamp and force gauge to measure stress–strain curves. Samples were initially 20 mm in length and were stretched at a rate of 4 mm/min until fracture occurred. Strain was calculated as the ratio of displacement to the original length, while stress was defined as the ratio of the applied load to the initial cross-sectional area of the sample. Three samples were prepared for each group, and three measurements were taken for each sample.

2.10 Degradation property analysis

In vitro degradation tests were conducted on the inner layer and the HB-NGC. The samples were initially weighed using an electronic balance to determine their starting weights. They were then immersed in PBS and maintained in a 37 °C environment. At predetermined time intervals, the samples were removed, rinsed with ultrapure water, dried in an oven at 54 °C for 2 h, and subsequently reweighed. The weight retention rate (r_{wr}) of the samples was calculated using the following equation:

$$r_{wr}=W_d/W_0\times100\%, \quad (1)$$

where W_0 is the initial weight and W_d is the weight after drying.

2.11 RSC96 cell culture

Rat Schwann cells (RSC96) were cultured in a complete medium consisting of 87% DMEM (4.5 g/L glucose), 10% FBS, 1% penicillin-streptomycin mixture, 1% L-alanyl-L-glutamine, and 1% sodium pyruvate. The cells were maintained in a humidified incubator at 37 °C with 5% CO_2. They were passaged when they reached 80% confluence. Depending on the specific experimental requirements, the cells were seeded in 96-well plates or 6-well plates.

2.12 Cell counting kit-8 (CCK-8) cell viability assay

Sterile NGC, NGC+HAMA, and NGC+HAMA (BMSCs) samples were cut into 1 mm^3 pieces and placed in 96-well plates. Then, 100 μL of RSC96 cell suspension at a density of 1×10^4 cells/mL was added to the experimental and control wells. After 3 and 5 d of culture, the medium was discarded, and 100 μL of a 10:100 mixture of CCK-8 reagent and complete medium was added to the experimental and control wells. Blank wells received the same volume of complete medium. The plates were then incubated in the dark for 4 h, and absorbance at 405 nm was measured using a microplate reader (Nivo, PerkinElmer, USA). Cell viability was calculated using the following equation:

$$\text{Cell viability} = \frac{A_{\text{test}} - A_{\text{blank}}}{A_{\text{control}} - A_{\text{blank}}} \times 100\%, \quad (2)$$

where A_{test}, A_{control}, and A_{blank} are the absorbance values of the experimental, control, and blank wells, respectively.

2.13 Cell migration

Prior to the experiment, parallel lines were marked on the bottom of a 6-well plate for positioning. RSC96 cells were then seeded into the 6-well plates at a density of 3×10^5 cells/well and cultured until a monolayer formed. A sterile 200 μL pipette tip was used to create uniform scratches perpendicular to the positioning lines on the cell monolayer. Sterile samples of NGC, NGC+HAMA, and NGC+HAMA (BMSCs) were placed into the wells and cultured further. Scratch images were captured at 0, 24, 48, and 72 h using an inverted fluorescence microscope (Eclipse Ti, Nikon, Japan). The cell migration rate (r_{cm}) was calculated using the following equation:

$$r_{\text{cm}} = \frac{S_0 - S_t}{S_0} \times 100\%, \quad (3)$$

where S_0 is the initial scratch area and S_t is the scratch area after t h of culture.

2.14 Cell morphology study

Sterile samples of NGC, NGC+HAMA, and NGC+HAMA (BMSCs) were placed into 6-well plates, where RSC96 cells were seeded at a density of 1×10^5 cells/cm^2. After 3 d of culture, the cells were stained for observation. The cells were fixed with 4% (volume fraction) paraformaldehyde for 30 min, followed by three washes with PBS (pH: 7.4). The cells were then permeabilized with 0.1% Triton X-100 for 5 min and washed three times with PBS. The cytoskeleton was then stained with phalloidin for 20 min, and the nuclei were stained with DAPI for 5 min. After each staining step, the samples were washed three times with PBS. Finally, the stained cells were observed using the inverted fluorescence microscope (Nikon).

2.15 Bio-functionality test of HAMA hydrogels

Transfer 100 μL of the precursor using a pipette onto a suitable curing ring (EFL-SCR-3D, EFL-Tech (Suzhou) Co., Ltd.) placed on a 48-well plate, for crosslinking as previously described. The resulting hydrogels were cultured for 48 h in a humidified incubator at 37 °C with 5% CO_2. After this period, they were stained using a live/dead cell double staining kit (KTA1001, Abbkine, China). In the staining results, dead cells appeared red, and live cells appeared green.

2.16 Paracrine capacity testing of BMSCs loaded in HAMA hydrogels

The culture supernatants containing BMSCs-loaded HAMA hydrogels were collected on Days 1, 3, 5, 7, and 10, and analyzed using rat vascular endothelial cell growth factor A (VEGF-A) using enzyme-linked immunosorbent assay (ELISA) kits (R2603c, Elabscience, China). Each time point included three replicates.

2.17 Animal surgery procedures

According to a well-accepted protocol, SD rats weighing approximately 250 g were used to create a 10-mm-long gap sciatic nerve injury model [44, 45]. A total of 16 animals were randomly divided into four groups (n=4 per group): autograft group, NGC group, NGC+HAMA group, and NGC+HAMA (BMSCs) group. Anesthesia was induced using isoflurane. The left hind limb of the rat was shaved, and a 1-cm longitudinal incision was made proximal to the knee joint to expose the muscle and underlying nerve tissue, allowing for isolation of the sciatic nerve. In the autograft group, a 10-mm segment of the sciatic nerve was excised and reattached in reverse orientation using 8-0 nylon sutures. In the other experimental groups, a 10-mm segment of the sciatic nerve was excised, and the NGC was sutured using 8-0 nylon. For the NGC+HAMA group, 0.2 mL of HAMA hydrogel was injected into the cavity of the NGC. For the NGC+HAMA (BMSCs) group, 0.2 mL of BMSCs-loaded HAMA hydrogel was injected into the cavity of the NGC. The muscle and skin were then sutured using 8-0 and 4-0 nylon sutures, respectively [6].

As the primary focus was on the design and fabrication of novel bionic nerve guidance conduits, the characterization was conducted according to protocols established in previous research [46–48].

2.18 Walking track analysis

In order to minimize the influence of variables such as animal motivation, stress, and varying walking speeds, particularly in rodent models, static gait indices such as the sciatic function index (SFI) and static sciatic index (SSI) were employed, following widely recognized and validated functional assessment protocols [11]. At 4, 8, and 12 weeks post-surgery, the rats were allowed to walk freely in a transparent corridor, with the hind limb footprints recorded below. Print length (l_p), toe spread (s_t), intermediate toe spread (s_{it}), and print width (w_p) were measured. The SFI was calculated as follows:

$$\mathrm{SFI} = 109.5 \times \frac{s_{et} - s_{nt}}{s_{nt}} - 38.3 \times \frac{l_{ep} - l_{np}}{l_{np}} + 13.3 \times \frac{s_{eit} - s_{nit}}{s_{nit}} - 8.8. \quad (4)$$

The SSI was calculated as follows:

$$\mathrm{SSI} = 108.44 \times \frac{s_{et} - s_{nt}}{s_{nt}} + 31.85 \times \frac{s_{eit} - s_{nit}}{s_{nit}} - 5.49. \quad (5)$$

Here, l_{ep}, s_{et}, and s_{eit} represent the experimental group's print length, toe spread, and intermediate toe spread, respectively. l_{np}, s_{nt}, and s_{nit} are the normal (uninjured) values for these parameters.

2.19 Gastrocnemius muscle testing

At 12 weeks post-surgery, after collecting the footprint data, all rats were euthanized, and the bilateral gastrocnemius muscles were collected and weighed. The wet weight ratio (r_{ww}) of the gastrocnemius muscle was calculated using the following equation:

$$r_{ww} = \frac{W_E}{W_N} \times 100\%, \quad (6)$$

where W_E is the wet weight of the operated side gastrocnemius muscle and W_N is the wet weight of the non-operated side gastrocnemius muscle.

2.20 Gastrocnemius muscle morphology analysis

The operated side gastrocnemius muscle was collected, fixed in 4% paraformaldehyde for 48 h, dehydrated in a series of ethanol gradients (75%, 85%, 95%, and 100%), embedded in paraffin, and then sectioned into 3-μm thick slices. These sections were stained with hematoxylin and eosin (H&E) and Masson trichrome. Muscle fiber cross-sectional area and collagen fiber percentage were measured using ImageJ software.

2.21 Regenerated nerve morphology analysis

The regenerated nerves from the surgical site were harvested, dehydrated using a sucrose solution gradient, and fixed in 4% paraformaldehyde for 2 h. The fixed nerves were embedded in optimal cutting temperature (OCT) compound (SAKURA, Japan) for toluidine blue (TB) staining and immunofluorescence analysis. Another portion of the fixed nerves was embedded in epoxy resin for transmission electron microscopy (TEM) imaging (Talos F200S, Thermo Fisher Scientific, USA). The OCT-embedded nerves were sectioned into 5-μm thick slices using a freezing microtome (CM3050S, LEICA, Germany) for TB staining and immunofluorescence analysis, while the epoxy resin-embedded nerves were sectioned into ultrathin (approximately 50 nm) slices using an ultramicrotome (EM KMR3, LEICA) for TEM imaging. For immunofluorescence staining, the sections were initially fixed in 4% paraformaldehyde for 10 min, followed by three washes with PBS for 5 min each. The sections were then blocked with 10-fold diluted serum at 37 °C for 30 min. After discarding the serum, the sections were divided into two groups and incubated overnight at 4 °C with S100 beta rabbit monoclonal antibody (1: 1000, Beyotime, China) and β-tubulin rabbit monoclonal antibody (1:10 000, Beyotime). Following another round of washing three times with PBS for 5 min each, the sections were incubated in the dark at room temperature (25 °C) for 2 h with Alexa Fluor 488-conjugated goat anti-rabbit immunoglobulin G (IgG; 1:500, Beyotime) and Alexa Fluor 555-conjugated donkey anti-rabbit IgG (1:500, Beyotime). Finally, the sections were stained with DAPI for 5 min and observed using a fluorescence microscope. Ultrathin sections were stained with lead citrate and uranyl acetate and observed under a transmission electron microscope [49].

2.22 Statistical analysis

All experiments were conducted in triplicate, and the results are presented as mean±standard deviation. Statistical differences between experimental groups were assessed using one-way analysis of variance (ANOVA). Significance levels are indicated as follows: $^{*}p<0.05$, $^{**}p<0.01$, $^{***}p<0.001$, and $^{****}p<0.0001$.

3 Results and discussion

3.1 Characterization of the HB-NGC

3.1.1 Morphological characterization

The morphology of the HB-NGC was investigated using a scanning electron microscope. Figures 2a and 2b show the photographs of the HB-NGC. The HB-NGC was 2 cm in length, with an inner diameter of 1.6 mm and an outer diameter of approximately 3 mm. Figure 2c shows the SEM image of the inner structure of the HB-NGC. EHD printing

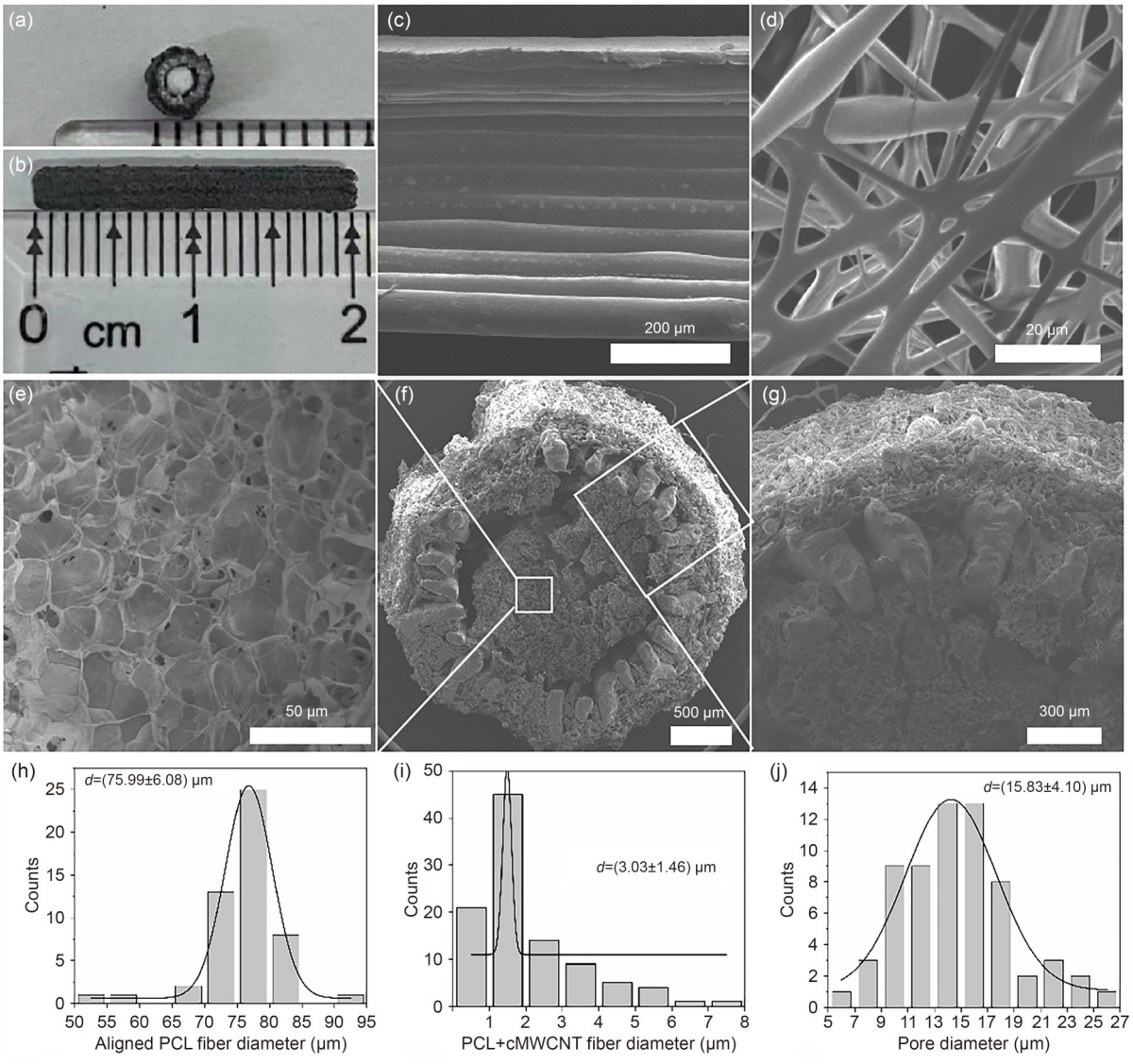

Fig. 2 Topography of HB-NGC. (a, b) Side and top views of the HB-NGC. (c) SEM image of the highly aligned PCL inner layer. (d) SEM image of electrospun PCL fibers loaded with cMWCNTs. (e) Porous microstructure of the HAMA hydrogel filler. (f) Cross-sectional view of the HB-NGC. (g) Enlarged local view of the HB-NGC. (h) Diameter distribution of the highly aligned PCL fibers in the inner layer. (i) Diameter distribution of the cMWCNT-loaded electrospun PCL fibers in the outer layer. (j) Pore size distribution of the HAMA hydrogel

technology allowed precise control over the orientation of fibers, and PCL fibers exhibited a highly aligned structure along the axis, resembling the structure of natural nerve bundles and guiding the direction of cell growth [50]. Figure 2d shows the SEM image of the outer layer of the HB-NGC. The nonuniform morphology of the electrospun cMWCNT-loaded PCL fibers may be attributed to the aggregation of cMWCNTs. As shown in Table S1 (supplementary information), the measured conductivity of PCL solution loading with 5% cMWCNTs was (749.3±6.3) μS/cm, which was significantly higher than that of pure PCL solution ((0.047± 0.015) μS/cm). The addition of cMWCNTs imparts conductivity to HB-NGC, mimicking the conduction of nerve sheath electrical signals, which is beneficial for nerve function repair [51]. The precursor solution was exposed to 405 nm light for 30 s, converting the precursor solution into HAMA hydrogels (Fig. S1 in the supplementary information). The HAMA hydrogel filled in the tubular core of HB-NGC demonstrated a porous structure (Fig. 2e), similar to the structure of natural ECM, promoting cell adhesion and growth [52]. Figure 2f shows the SEM image of the cross-section of HB-NGC. In the high-resolution image of Fig. 2g, it is clear that the HB-NGC has a three-layer structure. From the innermost to the outermost, it consists of HAMA filler, a highly aligned PCL inner layer, and an outer layer of cMWCNT-loaded PCL fibers. Meanwhile, the filler, inner layer (as shown in Fig. S2 in the supplementary information), and outer layer of HB-NGC all have pores, ensuring

nutrient exchange between the interior of HB-NGC and the external environment. Figure 2h shows the diameter of the highly aligned PCL fibers in the inner layer, with an average diameter of (75.99±6.08) μm, predominantly distributed within the range of 70–85 μm. Figure 2i demonstrates the diameter of the electrospun cMWCNT-loaded PCL fibers in the outer layer of HB-NGC, with an average diameter of (3.03±1.46) μm, with a more dispersed distribution as a result of cMWCNT aggregation. Figure 2j shows the pore size of the HAMA hydrogel filler, with an average pore size of (15.83±4.10) μm.

3.1.2 Fourier transform infrared spectroscopy analysis

The FTIR spectra of the materials were acquired to identify the distinctive functional groups and evaluate the chemical interactions among the various components. Figure 3a presents the FTIR spectra of PCL, cMWCNT, HAMA hydrogel, and NGC+HAMA. The cMWCNT exhibited a peak at 1735 cm^{-1} due to C=O stretching, a peak at 1034 cm^{-1} from C–O stretching vibration, and a peak at 3445 cm^{-1} attributed to –OH stretching vibration. Additionally, peaks at 2855 and 2927 cm^{-1} were due to the asymmetric and symmetric stretching of $–CH_2$ groups, respectively [53]. For pure PCL, the peaks at 2937 and 2860 cm^{-1} corresponded to the asymmetric and symmetric stretching of $–CH_2$, respectively, while the peak at 1721 cm^{-1} was due to C=O stretching, and the peak at 3300 cm^{-1} was related to the –NH group in PCL [54]. For HAMA hydrogel, the peaks at 1716 and 1499 cm^{-1} were attributed to C=O stretching and C=C bonds in methacrylate, respectively, while the peak at 1040 cm^{-1} was due to C–O–C bending vibration. Additionally, HAMA hydrogel contained –NH and $–CH_2$ groups, thus peaks were observed at 3300 and 2937 cm^{-1}, respectively [55]. The characteristic peaks of all materials are present in the NGC+HAMA sample, indicating that the preparation process did not alter the chemical structures of the materials, nor did it induce any reactions between them.

3.1.3 Water contact angle analysis

Water contact angle experiments were conducted on the inner layer, outer layer, and filler of the HB-NGC to assess the hydrophilicity of each part. As shown in Fig. 3b, the water contact angle of the outer layer of HB-NGC was 105.9°±7.0°, which was due to the hydrophobic nature of PCL. The water contact angle of the inner layer of HB-NGC was 67.6°±5.5°, showing hydrophilicity because droplets could diffuse into the gaps between the highly aligned fibers in the inner layer. The water contact angle of the HB-NGC was 0° (as shown in Fig. S3 in the supplementary information), as the HAMA hydrogel filling inside the HB-NGC was completely hydrophilic and could absorb and retain a large amount of water. The hydrophobic outer layer and the hydrophilic inner filler of the HB-NGC provided directional guidance for the liquid medium and a relatively closed

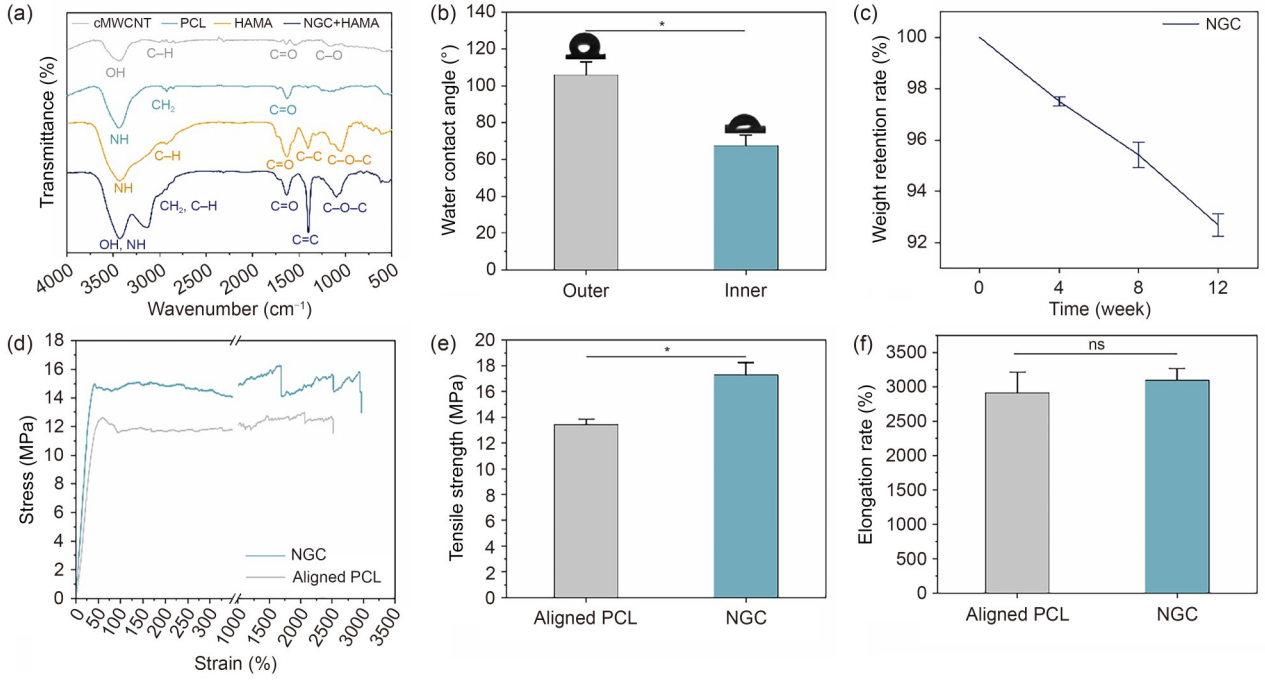

Fig. 3 Characterization of HB-NGC materials. (a) FTIR spectra of NGC+HAMA and its individual components. (b) Water contact angle analysis of the inner and outer layers. (c) In vitro degradation analysis of the NGC. (d) Mechanical performance analysis of the inner layer and the NGC. (e) Tensile strength comparison between the inner layer and the complete NGC. (f) Elongation rate of the inner layer and the complete NGC. Data in (b, c, e, f) are expressed as mean±standard deviation (n=3). $^{*}p<0.05$; ns: not significant

microenvironment for cells, which was beneficial for nerve regeneration.

3.1.4 Degradation and mechanical performance analysis

Excellent NGCs require good mechanical performance and slow degradation properties to maintain structure and functionality stably during transplantation and nerve regeneration processes. Therefore, the degradation and mechanical properties of the NGC were analyzed using in vitro degradation tests and axial tensile tests, respectively. The weight retention of the inner layer was minimal (Fig. S5 in the supplementary information). As shown in Fig. 3c, the weight retention rate of the NGC was (92.68±0.43)% at 12 weeks. This result indicates that HB-NGC does not degrade during the time of nerve repair. According to previous studies, high-molecular-weight PCL can completely degrade and be expelled from the body after three years of implantation [56]. Thus, this HB-NGC still had excellent degradability. Figure 3d depicts the stress–strain curves of the highly aligned PCL fibers and the NGC. Figure 3e shows that the tensile strengths of the highly aligned PCL fibers and the NGC were (13.4±0.5) and (17.3±0.9) MPa, respectively. The NGC exhibited higher tensile strength than the highly aligned PCL fibers, attributed to the effect of the electrospun cMWCNT-loaded PCL outer layer. From Fig. 3f, it can be seen that the elongation rates of the highly aligned PCL fibers in the inner layer and the NGC were (2916.1±302.9)% and (3100.1±168.3)%, respectively, with no significant difference between them. Due to the same base materials, there was no significant difference in Young's modulus between the two (as shown in Fig. S4 in the supplementary information). The tensile strength of the NGC ((17.3±0.9) MPa) was far greater than the ultimate stress of natural nerves (11.7 MPa), and it could support the mechanical requirements for nerve regeneration [34].

3.2 In vitro cell experiments

3.2.1 Verification of BMSCs' paracrine function

To validate that BMSCs maintained their paracrine function within HAMA hydrogel, live/dead staining of BMSCs in HAMA hydrogel was performed first. As shown in Fig. 4a, the viability of BMSCs was high, with minimal dead cells. However, due to HAMA hydrogel's low adhesion characteristics, BMSCs exhibited a round shape [52]. Quantitative analysis of VEGF-A was performed to verify the paracrine function of BMSCs in HAMA hydrogel. The cumulative release of VEGF-A by BMSCs over 1, 3, 5, 7, and 10 d was measured. As depicted in Fig. 4b, BMSCs continuously released VEGF-A, indicating that BMSCs can survive normally in HAMA hydrogel and maintain their paracrine function.

3.2.2 Cell fluorescence staining

To observe the effect of HB-NGC on cell morphology, RSC96 cells were stained with DAPI and phalloidin. As shown in Fig. 4c, RSC96 cells in the NGC, NGC+HAMA, and NGC+HAMA (BMSCs) groups grew along the highly aligned PCL fibers in the inner layer, indicating that the highly aligned PCL structure in the inner layer could guide the direction of cell growth, successfully mimicking the structure of nerve bundles.

3.2.3 Cell biocompatibility characterization

Figure 4d depicts the migration of RSC96 cells at 0, 24, 48, and 72 h after creating the scratch model. From the figure, it can be seen that over time, the cells migrated towards the central area. At each time point, the migration area of the NGC+HAMA (BMSCs) group was significantly larger than that of the other three groups. In Fig. 4e, the migration areas of each group were quantified. At 72 h, the migration rates were 92.3% for the control group, 91.4% for the NGC group, 95.5% for the NGC+HAMA group, and 97.7% for the NGC+HAMA (BMSCs) group. It can be observed that the migration rate of the NGC+HAMA (BMSCs) group was significantly higher than that of the other three groups. This indicates that HB-NGC had the best effect in promoting cell migration, which is beneficial for peripheral nerve repair.

The cytotoxicity of HB-NGC was evaluated using the CCK-8 assay. As shown in Fig. 4f, the cell viability of the NGC, NGC+HAMA, and NGC+HAMA (BMSCs) groups was all above 100% for RSC96 cells, demonstrating that HB-NGC had no cytotoxic effects and could promote cell proliferation. The cell viability of the NGC+HAMA (BMSCs) group was significantly higher than that of the other two experimental groups, possibly due to various growth factors secreted by BMSCs promoting cell proliferation.

3.3 Animal experiment on nerve injury

To evaluate the role of the HB-NGC in promoting sciatic nerve repair, hind limb footprints were collected at 4, 8, and 12 weeks, as shown in the experimental scheme (Fig. 5a). At 12 weeks, gastrocnemius muscle and regenerated nerve tissues were harvested for pathological staining and functional assessment. Figure 5b shows representative footprints from the left hind limb (injured side) of the rats. Within each group, toe spreading gradually increased over time. Among the three experimental groups, the NGC+HAMA (BMSCs) group exhibited the greatest degree of toe spreading. Quantitative analyses of the SSI and SFI are shown in Figs. 5c and 5d, respectively. At 12 weeks, the SFI values for the NGC, NGC+HAMA, NGC+HAMA (BMSCs), and autograft groups were −76.6±2.2, −66.5±5.3, −52.2±1.2, and −34.8±1.4,

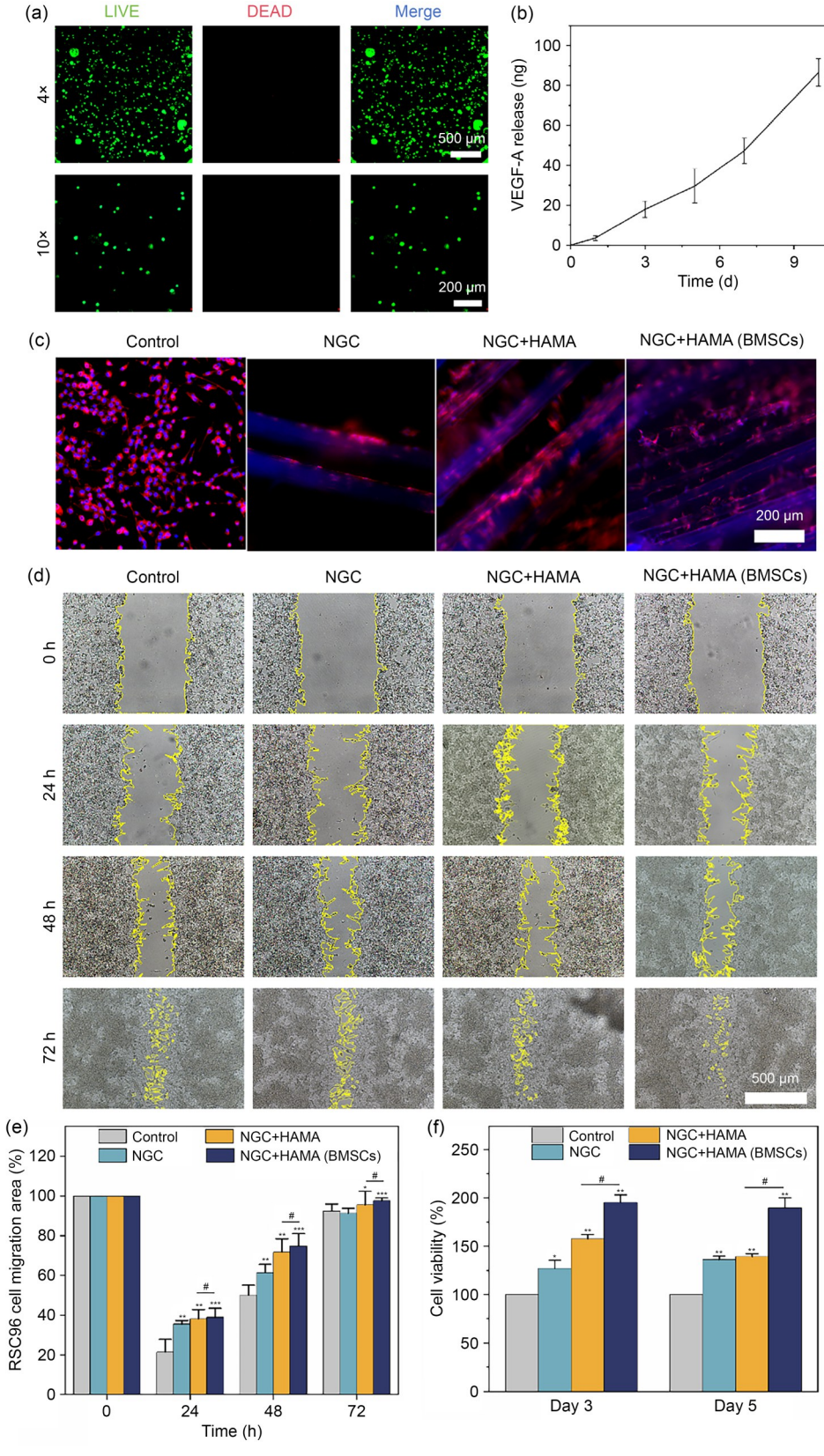

Fig. 4 HB-NGC biocompatibility testing. (a) Live/Dead staining of BMSCs encapsulated in HAMA hydrogel. (b) Cumulative release of VEGF-A. (c) DAPI and phalloidin staining of RSC96 cells. (d) Representative images of RSC96 cell migration in the scratch assay at 0, 24, 48, and 72 h. (e) Quantification of RSC96 cell migration area over time. (f) CCK-8 assay results showing cell viability in different treatment groups. Data in (b, e, f) are expressed as mean±standard deviation (n=3). $^{*}p<0.05$, $^{**}p<0.01$, $^{***}p<0.001$, and $^{\#}p<0.05$

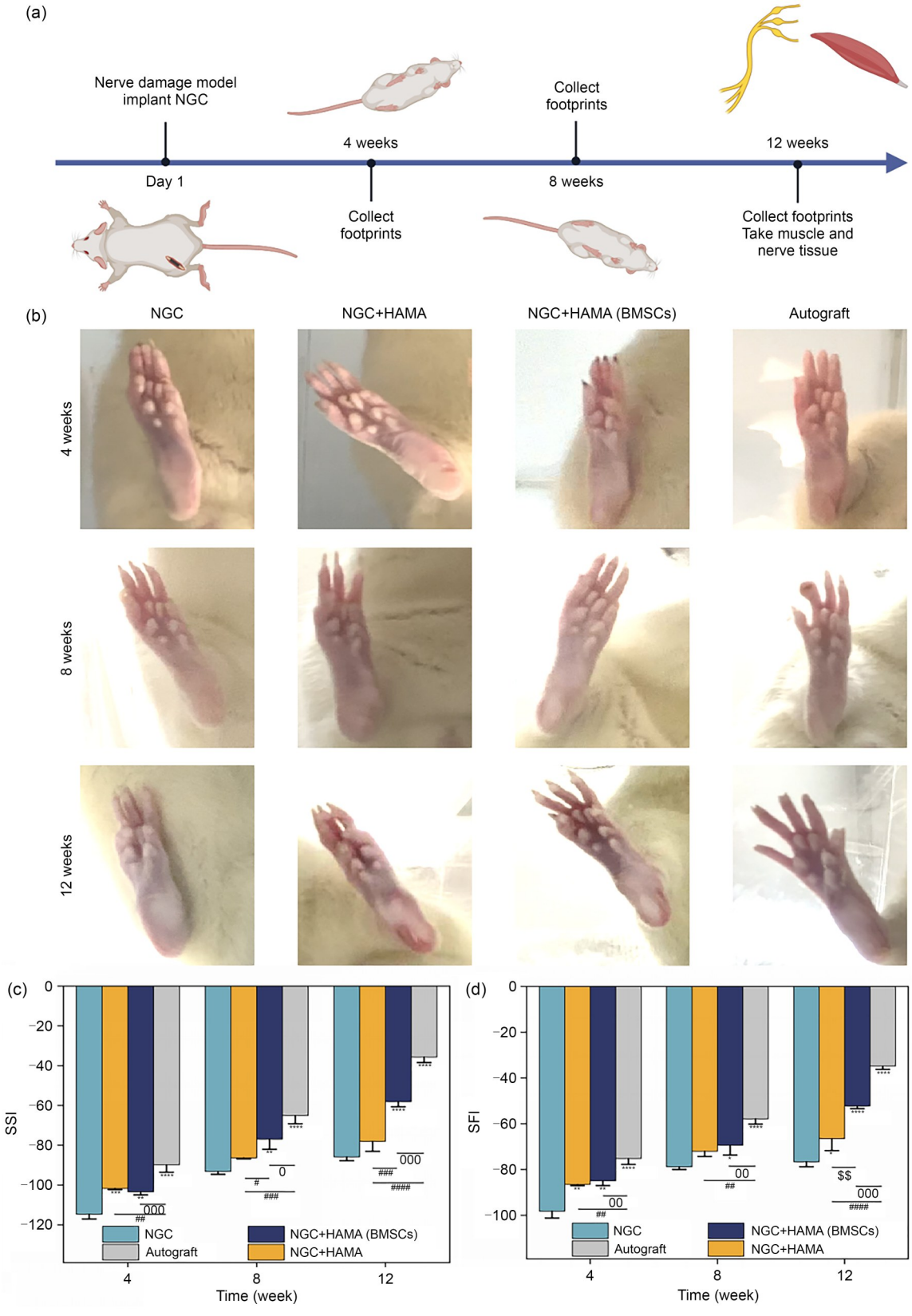

Fig. 5 Gait analysis. (a) Schematic diagram of the experimental timeline following implantation of nerve conduits. (b) Representative hind limb footprints collected at 4, 8, and 12 weeks post-surgery. Quantitative analysis of the SSI (c) and SFI (d) over time. Data in (c, d) are expressed as mean±standard deviation (n=3). $^{*}p<0.05$, $^{**}p<0.01$, $^{***}p<0.001$, $^{****}p<0.0001$, $^{\#}p<0.05$, $^{\#\#}p<0.01$, $^{\#\#\#}p<0.001$, $^{\#\#\#\#}p<0.0001$, $^{0}p<0.05$, $^{00}p<0.01$, $^{000}p<0.001$, and $^{\$\$}p<0.01$

respectively. The corresponding SSI values were −85.8±1.9, −78.0±5.0, −58.1±2.6, and −35.7±2.8. These results indicate that the NGC+HAMA (BMSCs) group significantly outperformed the other two experimental groups and approached the functional recovery observed in the autograft group, suggesting a superior repair effect.

S100 and β-tubulin are specific markers for Schwann cells and the main structural protein in axons, respectively. Immunofluorescence staining for S100 and β-tubulin was performed on cross-sections of the regenerated nerves to analyze nerve regeneration. Figures 6a and 6b show that the NGC+HAMA (BMSCs) group had the largest fluorescent area among the experimental groups. The fluorescent area percentages for β-tubulin in Fig. 6d were (75.7±0.8)% for the autograft group, (51.4±1.0)% for the NGC group, (65.2±1.0)% for the NGC+HAMA group, and (71.5±0.8)% for the NGC+HAMA (BMSCs) group. Figure 6c shows the quantitative results of the fluorescent area for S100, with (71.5±0.5)% for the autograft group, (45.6±0.9)% for the NGC group, (55.2±1.1)% for the NGC+HAMA group, and (64.1±0.2)% for the NGC+HAMA (BMSCs) group. Significant discrepancies were noted across all groups, with the NGC+HAMA (BMSCs) group markedly outperforming the NGC and NGC+HAMA groups, closely mirroring the outcomes of the autograft group. This suggests that the paracrine effect of BMSCs effectively fosters nerve regeneration. Additionally, the combined effects of the inner layer (which mimics the nerve bundle structure), the outer layer (which facilitates nerve signal conduction), the HAMA hydrogel (which replicates the ECM), and the paracrine function of BMSCs work together to closely replicate natural nerves and promote nerve regeneration.

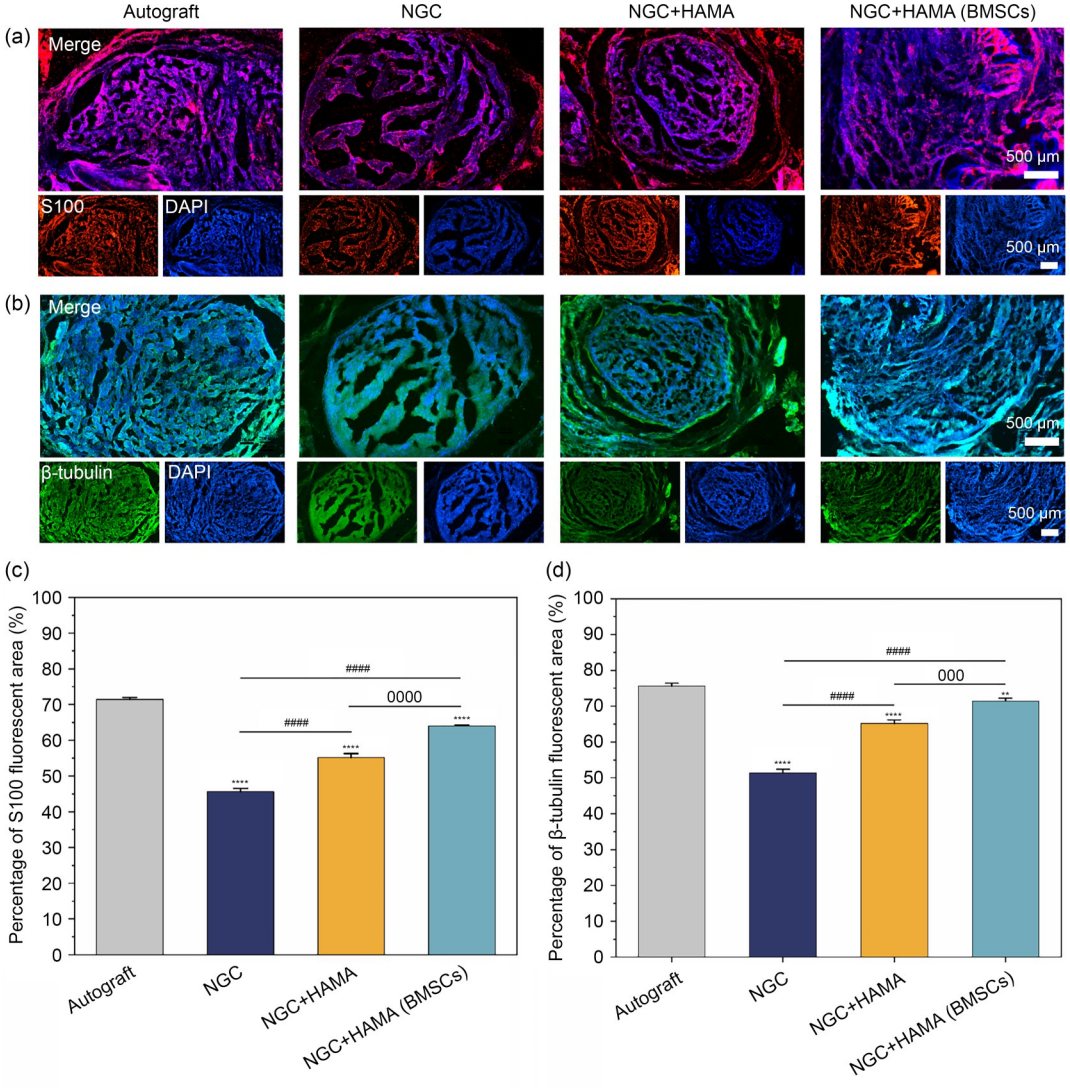

Fig. 6 Protein fluorescence staining analysis. (a) Immunofluorescence staining of regenerated nerve cross-sections for S100. (b) Immunofluorescence staining of regenerated nerve cross-sections for β-tubulin. (c) Quantification of S100-positive area. (d) Quantification of β-tubulin-positive area. Data in (c, d) are expressed as mean±standard deviation (n=3). $^{**}p<0.01$, $^{****}p<0.0001$, $^{\#\#\#\#}p<0.0001$, $^{000}p<0.001$, and $^{0000}p<0.0001$

Figure 7a shows the morphology of regenerated nerves and HB-NGC at 12 weeks, showing that HB-NGC maintained good structural integrity. Throughout the entire repair process, HB-NGC consistently provided mechanical support for the regenerating nerves (Fig. S6 in the supplementary information). TB staining was performed on regenerated nerves, with the staining solution used to stain the myelin sheaths, as shown in Fig. 7b. All experimental groups displayed myelin sheath formation in the regenerated nerves, with the NGC+HAMA (BMSCs) group showing significantly better myelin sheath formation compared to the other two experimental groups. Figure 7d presents a quantitative analysis of the myelin sheath area. The NGC+HAMA (BMSCs) group exhibited a myelin expression area of (54.2±1.0)%, significantly better than the NGC group (34.0±1.5)% and the NGC+HAMA group (46.1±0.7)%. This result was closest to the autograft group, which had a myelin expression area of (82.9±0.7)%. The cross-section of regenerated nerves was imaged using a transmission electron microscope to further analyze myelin sheath formation. As shown in Fig. 7c, among the experimental groups, the regenerated nerve diameter and myelin sheath thickness in the NGC+HAMA (BMSCs) group were closest to those in the autograft group. The NGC group exhibited smaller regenerated nerve diameters and thinner myelin sheaths, while the NGC+HAMA group showed some improvement but still fell short of the repair outcomes observed in the NGC+HAMA (BMSCs) group. Figure 7e quantifies the diameter of the myelinated nerves as follows: (4.1±0.1) μm in the autograft group, (2.4±0.2) μm in the NGC group, (3.0±0.3) μm in the NGC+HAMA group, and (3.5±0.1) μm in the NGC+HAMA (BMSCs) group. The myelinated nerve diameter in the NGC+HAMA (BMSCs) group was closest to that of the autograft group. Figure 7f illustrates the myelin sheath thickness for each group: (0.58±0.01) μm for the autograft group, (0.39±0.04) μm for the NGC group, (0.39±0.02) μm for the NGC+HAMA group, and (0.57±0.01) μm for the NGC+HAMA (BMSCs) group. These results indicate that HB-NGC has a significant effect on nerve regeneration and myelination.

The condition of gastrocnemius muscle atrophy, muscle fiber diameter, and collagen deposition can reflect the level of functional reconstruction of the sciatic nerve. As shown in Fig. 8a, the volume of the left gastrocnemius muscle in all groups was smaller than that of the right normal gastrocnemius muscle, indicating varying degrees of atrophy in all groups. Among the three experimental groups, the NGC+HAMA (BMSCs) group exhibited the mildest muscle atrophy. H&E and Masson staining were performed on the left hind limb gastrocnemius muscle of rats to further evaluate nerve function recovery. As shown in Fig. 8b, Masson staining revealed the highest collagen deposition in the NGC group, while the NGC+HAMA (BMSCs) group and the autograft group showed the least collagen deposition.

Figure 8c presents the pathological image of the gastrocnemius muscle stained with H&E, demonstrating that, compared to the NGC group and NGC+HAMA group, the NGC+HAMA (BMSCs) group exhibited more regular muscle tissue and a denser distribution of muscle fibers. Figure 8d illustrates the quantitative results of the wet weight ratio of the gastrocnemius muscle. The autograft group, NGC group, NGC+HAMA group, and NGC+HAMA (BMSCs) group exhibited ratios of (69.3±7.4)%, (31.3±5.8)%, (47.1±5.2)%, and (63.2±8.6)%, respectively. The NGC+HAMA (BMSCs) group showed no significant difference from the autograft group but was significantly higher than the other two experimental groups, indicating that HB-NGC can effectively improve muscle atrophy.

Figure 8e presents the quantitative analysis of muscle fiber diameter, with diameters of (82.8±11.3) μm for the autograft group, (63.1±13.7) μm for the NGC group, (63.6±11.0) μm for the NGC+HAMA group, and (78.6±10.9) μm for the NGC+HAMA (BMSCs) group. The muscle fiber diameter in the NGC+HAMA (BMSCs) group was significantly better than in the other two experimental groups, suggesting that encapsulation of mesenchymal stem cells is critical for soft tissue regeneration. Figure 8f shows the collagen fiber area percentage of the autograft group, NGC group, NGC+HAMA group, and NGC+HAMA (BMSCs) group as (6.1±0.4)%, (16.1±0.7)%, (9.1±0.6)%, and (4.6±0.4)%, respectively. Additionally, the collagen deposition in the NGC+HAMA (BMSCs) group was significantly lower than in the other two experimental groups, approaching the level of the autograft group. Furthermore, significant differences were observed among the NGC group, NGC+HAMA group, and NGC+HAMA (BMSCs) group, indicating that the highly biomimetic microenvironment provided by the HB-NGC effectively promoted nerve repair and significantly enhanced nerve function reconstruction.

4 Conclusions

In this study, we successfully developed the HB-NGC using a hybrid high-voltage electrotechnology that combined electrospinning and EHD printing technologies. The prepared HB-NGC closely mimicked natural nerves by restoring the physical pathway, bridging electrical signal conduction, replicating nerve bundle structures, and providing an ECM environment along with essential growth factors between the severed ends of a nerve. Additionally, the HB-NGC demonstrated slow degradation, robust mechanical properties, and exceptional biocompatibility, all of which support peripheral nerve regeneration. Both in vivo and in vitro experiments confirmed significant efficacy in promoting nerve regeneration and functional recovery. The highly aligned inner layer of the HB-NGC replicated the natural nerve

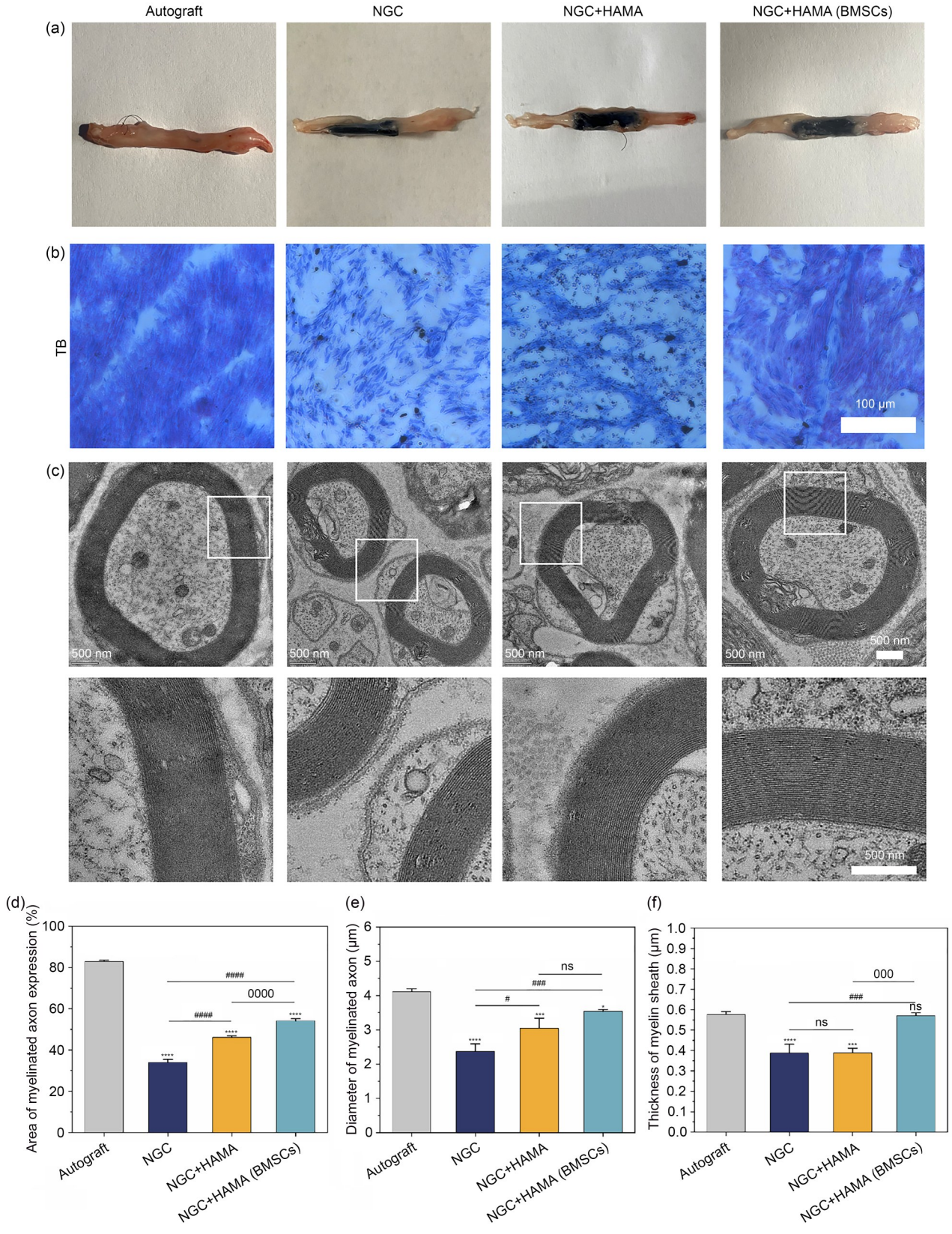

Fig. 7 Regenerative nerve myelin analysis. (a) Morphology of the regenerated nerves and the HB-NGC at 12 weeks. (b) TB staining of regenerated nerves. (c) TEM images of cross-sections of regenerated nerves. Quantitative analysis of myelin sheath area (d), diameter of myelinated axons (e), and myelin sheath thickness (f) in each group. Data in (d–f) are expressed as mean±standard deviation (n=3). $^{*}p<0.05$, $^{***}p<0.001$, $^{****}p<0.0001$, $^{\#}p<0.05$, $^{\#\#\#}p<0.001$, $^{\#\#\#\#}p<0.0001$, $^{000}p<0.001$, and $^{0000}p<0.0001$; ns: not significant

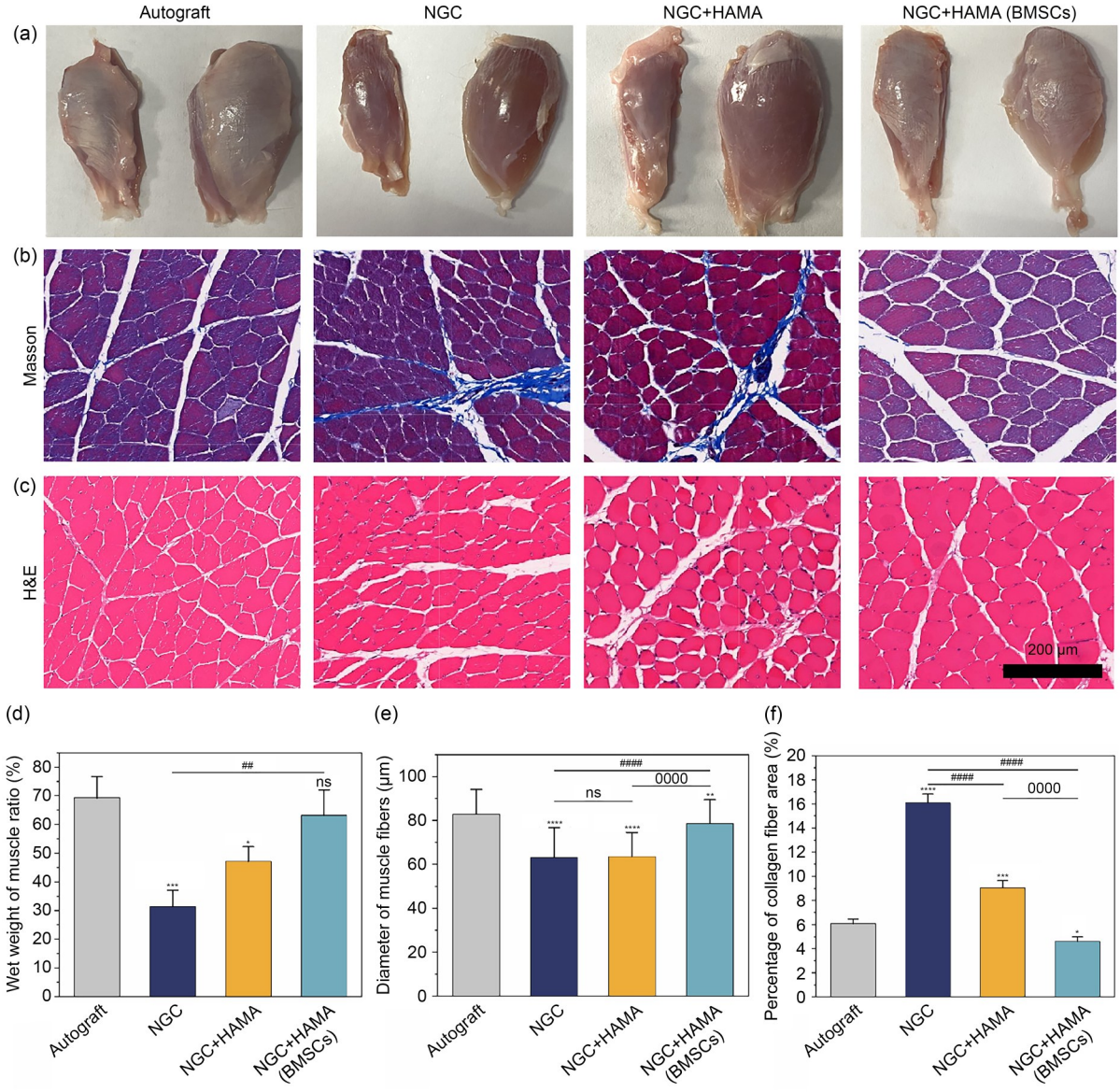

Fig. 8 Gastrocnemius muscle staining analysis. (a) Comparison between the operated-side and normal gastrocnemius muscles. (b) Masson staining of the gastrocnemius muscle. (c) H&E staining of the gastrocnemius muscle. (d) Wet weight ratio of the gastrocnemius muscle. (e) Muscle fiber diameter of the gastrocnemius muscle. (f) Collagen deposition area in the gastrocnemius muscle. Data in (d–f) are expressed as mean±standard deviation (n=3). $^{*}p<0.05$, $^{**}p<0.01$, $^{***}p<0.001$, $^{****}p<0.0001$, $^{\#\#}p<0.01$, $^{\#\#\#\#}p<0.0001$, and $^{0000}p<0.0001$; ns: not significant

bundle structure, guiding the direction of regenerated nerve growth. Nerve and muscle staining results indicated that higher biomimetic levels led to better recovery of muscle and nerve functions, approaching the results of autograft groups. Overall, this study underscores the remarkable potential of the HB-NGC to support and guide the microenvironment in the regrowth of injured nerves.

Supplementary Information The online version contains supplementary material available at https://doi.org/10.1631/bdm.2500026.

Acknowledgements This work was supported by the Natural Science Foundation of Hebei Province of China (Nos. H2020202002 and H2023202001), the Natural Science Foundation of Tianjin City of China (No. 24JCQNJC01180), and Science Research Project of Hebei Educational Department (No. BJK2023034).

Author contributions CL: investigation, methodology, data curation, formal analysis, writing; LFZ: investigation, methodology, revising, and editing; MWC: supervision, methodology, revising, and editing; HL: methodology and writing; SHL: methodology and validation; BLW: conceptualization, supervision, funding acquisition, methodology, revising, and editing.

Declarations

Conflict of interest The authors declare that they have no known competing financial interests or personal relationships that could have appeared to influence the work reported in this paper.

Ethical approval All animal procedures were conducted in accordance with the guidelines approved by the Biomedical Ethics Committee of Hebei University of Technology (approval number: HEBUTACUC2023049).

Data availability The data that support the findings of this study are available from the corresponding authors upon reasonable request.

References

1. Xu DY, Fu SQ, Zhang H et al (2024) Ultrasound-responsive aligned piezoelectric nanofibers derived hydrogel conduits for peripheral nerve regeneration. Adv Mater 36(28):2307896. https://doi.org/10.1002/adma.202307896
2. Xue W, Shi W, Kong YF et al (2021) Anisotropic scaffolds for peripheral nerve and spinal cord regeneration. Bioact Mater 6(11): 4141–4160. https://doi.org/10.1016/j.bioactmat.2021.04.019
3. Li JJ, Yao YX, Wang Y et al (2022) Modulation of the crosstalk between Schwann cells and macrophages for nerve regeneration: a therapeutic strategy based on a multifunctional tetrahedral framework nucleic acids system. Adv Mater 34(46):2202513. https://doi.org/10.1002/adma.202202513
4. Song JH, Dong JZ, Yuan ZC et al (2024) Shape-persistent conductive nerve guidance conduits for peripheral nerve regeneration. Adv Healthc Mater 13(26):2401160. https://doi.org/10.1002/adhm.202401160
5. Wei ZD, Jin F, Li T et al (2023) Physical cue-based strategies on peripheral nerve regeneration. Adv Funct Mater 33(3):2209658. https://doi.org/10.1002/adfm.202209658
6. Seong D, Choi Y, Choi IC et al (2024) Sticky and strain-gradient artificial epineurium for sutureless nerve repair in rodents and nonhuman primates. Adv Mater 36(16):2307810. https://doi.org/10.1002/adma.202307810
7. Zhang M, An H, Gu Z et al (2023) Multifunctional wet-adhesive chitosan/acrylic conduit for sutureless repair of peripheral nerve injuries. Int J Biol Macromol 253:126793. https://doi.org/10.1016/j.ijbiomac.2023.126793
8. Lan DW, Wu BQ, Zhang HQ et al (2023) Novel bioinspired nerve scaffold with high synchrony between biodegradation and nerve regeneration for repair of peripheral nerve injury. Biomacromolecules 24(11):5451–5466. https://doi.org/10.1021/acs.biomac.3c00920
9. Zhou WX, Rahman MSU, Sun CM et al (2024) Perspectives on the novel multifunctional nerve guidance conduits: from specific regenerative procedures to motor function rebuilding. Adv Mater 36(14):2307805. https://doi.org/10.1002/adma.202307805
10. Antman-Passig M, Giron J, Karni M et al (2021) Magnetic assembly of a multifunctional guidance conduit for peripheral nerve repair. Adv Funct Mater 31(29):2010837. https://doi.org/10.1002/adfm.202010837
11. Liu SH, Zhu LF, Chang MW et al (2025) Magnetic field-assisted conductive nerve guidance conduit enabling peripheral nerve regeneration with wireless electrical stimulation. Adv Funct Mater 2416548. https://doi.org/10.1002/adfm.202416548
12. Zhang CY, Gong JX, Zhang JY et al (2023) Three potential elements of developing nerve guidance conduit for peripheral nerve regeneration. Adv Funct Mater 33(40):2302251. https://doi.org/10.1002/adfm.202302251
13. Sun RY, Wang BL, Zhang LF et al (2022) Engineering three-dimensional bendable helix conduits for peripheral nerve regeneration via hybrid electrotechnologies. ACS Mater Lett 4(11): 2210–2218. https://doi.org/10.1021/acsmaterialslett.2c00698
14. Liu CD, Sun MY, Lin LN et al (2025) Potentially commercializable nerve guidance conduits for peripheral nerve injury: past, present, and future. Mater Today Bio 31:101503. https://doi.org/10.1016/j.mtbio.2025.101503
15. Rao F, Wang YH, Zhang DY et al (2020) Aligned chitosan nanofiber hydrogel grafted with peptides mimicking bioactive brain-derived neurotrophic factor and vascular endothelial growth factor repair long-distance sciatic nerve defects in rats. Theranostics 10(4):1590–1603. https://doi.org/10.7150/thno.36272
16. Han YY, Yang JX, Fang JK et al (2022) The secretion profile of mesenchymal stem cells and potential applications in treating human diseases. Signal Transduct Target Ther 7(1):92. https://doi.org/10.1038/s41392-022-00932-0
17. Huang YY, Ye K, He AD et al (2024) Dual-layer conduit containing VEGF-A–transfected Schwann cells promotes peripheral nerve regeneration via angiogenesis. Acta Biomater 180:323–336. https://doi.org/10.1016/j.actbio.2024.03.029
18. Wang J, Xiong H, Zhu TH et al (2020) Bioinspired multichannel nerve guidance conduit based on shape memory nanofibers for potential application in peripheral nerve repair. ACS Nano 14(10):12579–12595. https://doi.org/10.1021/acsnano.0c03570
19. Zhang H, Xu DY, Zhang B et al (2024) PEDOT-integrated fish swim bladders as conductive nerve conduits. Adv Sci 11(31): 2400827. https://doi.org/10.1002/advs.202400827
20. Liu K, Yan LS, Li RT et al (2022) 3D printed personalized nerve guide conduits for precision repair of peripheral nerve defects. Adv Sci 9(12):2103875. https://doi.org/10.1002/advs.202103875
21. Hu YN, Chen ZY, Wang HY et al (2022) Conductive nerve guidance conduits based on *Morpho* butterfly wings for peripheral nerve repair. ACS Nano 16(2):1868–1879. https://doi.org/10.1021/acsnano.1c11627
22. Ma Y, Wang H, Wang QQ et al (2023) Piezoelectric conduit combined with multi-channel conductive scaffold for peripheral nerve regeneration. Chem Eng J 452:139424. https://doi.org/10.1016/j.cej.2022.139424
23. Zhao RL, Jiang LH, Du J et al (2022) Fluffy sponge-reinforced electrospun conduits with biomimetic structures for peripheral nerve repair. Compos Part B Eng 230:109482. https://doi.org/10.1016/j.compositesb.2021.109482
24. Moreira A, Lawson D, Onyekuru L et al (2021) Protein encapsulation by electrospinning and electrospraying. J Control Release 329:1172–1197. https://doi.org/10.1016/j.jconrel.2020.10.046
25. Song S, Li C, Xiao Y et al (2025) Beyond conventional therapies: MSCs in the battle against nerve injury. Regen Ther 28:280–291. https://doi.org/10.1016/j.reth.2024.12.017
26. Zou XF, Zhang BZ, Qian WW et al (2024) Bone marrow mesenchymal stem cells in treatment of peripheral nerve injury. World J Stem Cells 16(8):799–810.

https://doi.org/10.4252/wjsc.v16.i8.799
27. Zhang XX, Zhang WW, Sun H et al (2024) The effects of exosomes originating from different cell sources on the differentiation of bone marrow mesenchymal stem cells into Schwann cells. J Nanobiotechnol 22(1):220. https://doi.org/10.1186/s12951-024-02450-3
28. Gong MH, Yan F, Yu L et al (2022) A dopamine-methacrylated hyaluronic acid hydrogel as an effective carrier for stem cells in skin regeneration therapy. Cell Death Dis 13(8):738. https://doi.org/10.1038/s41419-022-05060-9
29. Baker LA, Xu LL, Akher FB et al (2022) Nerve growth factor-binding engineered silk films promote neuronal attachment and neurite outgrowth. Adv Funct Mater 32(45):2205178. https://doi.org/10.1002/adfm.202205178
30. Liu MS, Zhang WC, Han SW et al (2024) Multifunctional conductive and electrogenic hydrogel repaired spinal cord injury via immunoregulation and enhancement of neuronal differentiation. Adv Mater 36(21):2313672. https://doi.org/10.1002/adma.202313672
31. Gao C, Li YX, Liu XY et al (2023) 3D bioprinted conductive spinal cord biomimetic scaffolds for promoting neuronal differentiation of neural stem cells and repairing of spinal cord injury. Chem Eng J 451:138788. https://doi.org/10.1016/j.cej.2022.138788
32. Wu P, Chen P, Xu C et al (2022) Ultrasound-driven in vivo electrical stimulation based on biodegradable piezoelectric nanogenerators for enhancing and monitoring the nerve tissue repair. Nano Energy 102:107707. https://doi.org/10.1016/j.nanoen.2022.107707
33. Yang YF, Yin X, Wang HD et al (2023) Engineering a wirelessly self-powered and electroconductive scaffold to promote peripheral nerve regeneration. Nano Energy 107:108145. https://doi.org/10.1016/j.nanoen.2022.108145
34. Sun RY, Lang YN, Chang MW et al (2024) Leveraging oriented lateral walls of nerve guidance conduit with core–shell MWCNTs fibers for peripheral nerve regeneration. Adv Healthc Mater 13(13): 2303867. https://doi.org/10.1002/adhm.202303867
35. Saranya M, da Silva AM, Karjalainen H et al (2023) Magnetic-responsive carbon nanotubes composite scaffolds for chondrogenic tissue engineering. Adv Healthc Mater 12(30):2301787. https://doi.org/10.1002/adhm.202301787
36. Saranya M, Koivisto JT, Carvalho ACM et al (2023) Aligned multi-walled carbon nanotube-embodied hydrogel via low magnetic field: a strategy for engineering aligned injectable scaffolds. Compos Part B Eng 248:110398. https://doi.org/10.1016/j.compositesb.2022.110398
37. Chang WT, Chen LR, Chen KH (2024) The bioengineering application of hyaluronic acid in tissue regeneration and repair. Int J Biol Macromol 270(Pt 2):132454. https://doi.org/10.1016/j.ijbiomac.2024.132454
38. Walvekar P, Lulinski P, Kumar P et al (2024) A review of hyaluronic acid-based therapeutics for the treatment and management of arthritis. Int J Biol Macromol 264:130645. https://doi.org/10.1016/j.ijbiomac.2024.130645
39. Tavakoli S, Krishnan N, Mokhtari H et al (2024) Fine-tuning dynamic cross–linking for enhanced 3D bioprinting of hyaluronic acid hydrogels. Adv Funct Mater 34(4):2307040. https://doi.org/10.1002/adfm.202307040
40. Jensen C, Teng Y (2020) Is it time to start transitioning from 2D to 3D cell culture? Front Mol Biosci 7:33. https://doi.org/10.3389/fmolb.2020.00033
41. Wu XY, Huang DQ, Xu Y et al (2023) Microfluidic templated stem cell spheroid microneedles for diabetic wound treatment. Adv Mater 35(28):2301064. https://doi.org/10.1002/adma.202301064
42. Shan YZ, Xu LL, Cui X et al (2025) A neurodevelopment-inspired self-evolving scaffold for nerve regeneration. Cell Biomater 1(1): 100006. https://doi.org/10.1016/j.celbio.2024.100006
43. Li MY, Yu YJ, Xue K et al (2023) Genistein mitigates senescence of bone marrow mesenchymal stem cells via ERRα-mediated mitochondrial biogenesis and mitophagy in ovariectomized rats. Redox Biol 61:102649. https://doi.org/10.1016/j.redox.2023.102649
44. Han Q, Guan WC, Sun SL et al (2024) Anisotropic topological scaffolds synergizing non-invasive wireless magnetic stimulation for accelerating long-distance peripheral nerve regeneration. Chem Eng J 496:153809. https://doi.org/10.1016/j.cej.2024.153809
45. Xiaohalati X, Wang J, Su QF et al (2024) A materiobiology-inspired sericin nerve guidance conduit extensively activates regeneration-associated genes of Schwann cells for long-gap peripheral nerve repair. Chem Eng J 483:149235. https://doi.org/10.1016/j.cej.2024.149235
46. Fan N, Song D, Ding HR et al (2025) E-jet 3D printed aligned nerve guidance conduits incorporated with decellularized extracellular matrix hydrogel encapsulating extracellular vesicles for peripheral nerve repair. Acta Biomater 194:122–139. https://doi.org/10.1016/j.actbio.2025.01.025
47. Chen X, Ge XM, Qian Y et al (2020) Electrospinning multilayered scaffolds loaded with melatonin and Fe_3O_4 magnetic nanoparticles for peripheral nerve regeneration. Adv Funct Mater 30(38): 2004537. https://doi.org/10.1002/adfm.202004537
48. Li T, Cheng QH, Zhang JG et al (2025) A novel flexible nerve guidance conduit promotes nerve regeneration while providing excellent mechanical properties. Neural Regen Res 20(7):2084–2094. https://doi.org/10.4103/NRR.NRR-D-23-01792
49. Kong LC, Gao X, Yao XY et al (2024) Multilevel neurium-mimetic individualized graft via additive manufacturing for efficient tissue repair. Nat Commun 15(1):6428. https://doi.org/10.1038/s41467-024-49980-w
50. Fang YC, Wang CJ, Liu ZB et al (2023) 3D printed conductive multiscale nerve guidance conduit with hierarchical fibers for peripheral nerve regeneration. Adv Sci 10(12):2205744. https://doi.org/10.1002/advs.202205744
51. Rahman M, Mahady Dip T, Padhye R et al (2023) Review on electrically conductive smart nerve guide conduit for peripheral nerve regeneration. J Biomed Mater Res Part A 111(12):1916–1950. https://doi.org/10.1002/jbm.a.37595
52. Yu KX, Huangfu HM, Qin QY et al (2022) Application of bone marrow-derived macrophages combined with bone mesenchymal stem cells in dual-channel three-dimensional bioprinting scaffolds for early immune regulation and osteogenic induction in rat calvarial defects. ACS Appl Mater Interfaces 14(41):47052–47065. https://doi.org/10.1021/acsami.2c13557
53. Zhao ZY, Yang ZH, Hu YW et al (2013) Multiple functionalization of multi-walled carbon nanotubes with carboxyl and amino groups. Appl Surf Sci 276:476–481. https://doi.org/10.1016/j.apsusc.2013.03.119
54. Tolou NB, Salimijazi H, Kharaziha M et al (2021) A three-dimensional nerve guide conduit based on graphene foam/polycaprolactone. Mater Sci Eng C 126:112110. https://doi.org/10.1016/j.msec.2021.112110
55. Aycan D, Karaca F, Koca A et al (2023) Electro-stimulated drug release by methacrylated hyaluronic acid-based conductive hydrogel with enhanced mechanical properties. Int J Biol Macromol 231:123297. https://doi.org/10.1016/j.ijbiomac.2023.123297
56. Sun HF, Mei L, Song CX et al (2006) The in vivo degradation, absorption and excretion of PCL-based implant. Biomaterials 27(9):1735–1740. https://doi.org/10.1016/j.biomaterials.2005.09.019